Chapter 4

Numerical modelling

This chapter considers the *Elastodynamic Finite Integration Technique* EFIT, partly developed in [47], as a solution to the elastodynamic equations. The numerical approach will be developed with a number of references to the original work [47]. Furthermore, the chapter discusses boundary conditions as well as how transducers may be modelled by specifying the traction vector at the contact surface together with suitable pulse signals. A simple model of a receiver is also discussed. Extensive use of tensor notation is used in [47] during the development of the theory. Here, the more reader friendly matrix notation will be used where possible.

4.1 Description of the discretization grids

Consider a volume V with surface S contained in the interior of a material under the influence of internal stresses $\sigma_{ij}(\boldsymbol{x}, t)$ but with body forces (such as gravitation) neglected. Performing a volume integration of the equation of motion (2.10) and transforming the volume integration on the righthand side to a surface integral using Gauss' theorem, we obtain

$$\int_V \rho(\boldsymbol{x})\dot{v}_i(\boldsymbol{x}, t)\,\mathrm{d}V = \int_S \sigma_{ij}(\boldsymbol{x}, t) n_j\,\mathrm{d}S, \qquad i = 1, 2, 3. \tag{4.1}$$

Here, $v_i = \dot{u}_i$ denotes the time derivative of the deformation components u_i introduced earlier. The dependence of position $\boldsymbol{x}$ and time t has been emphasized in the equation. This dependence exists throughout the chapter but will be suppressed in certain less important equations for reasons of clarity and space.

The volume integral of the time derivative of a strain component $\dot{\epsilon_{ij}}$ (section 2.2) may be transformed into a surface integral using Gauss' theorem in the following way

$$\begin{aligned}
\int_V \dot{\epsilon}_{ij}\,\mathrm{d}V &\equiv \frac{1}{2}\int_V (v_{i,j} + v_{j,i})\,\mathrm{d}V \\
&= \frac{1}{2}\int_V \left(\nabla\cdot(v_i\boldsymbol{e}_j) + \nabla\cdot(v_j\boldsymbol{e}_i)\right)\,\mathrm{d}V \\
&= \frac{1}{2}\int_S (v_j\boldsymbol{e}_i\cdot\boldsymbol{n} + v_i\boldsymbol{e}_j\cdot\boldsymbol{n})\,\mathrm{d}S \\
&= \frac{1}{2}\int_S (v_j n_i + v_i n_j)\,\mathrm{d}S
\end{aligned} \tag{4.2}$$

using (2.4). Here, $\boldsymbol{n}$ denotes an outward normal vector to S. Using this result together with Hooke's law (2.20), the deformation rate equation is obtained

$$\int_V \boldsymbol{s}(\boldsymbol{x}) \begin{pmatrix} \dot{\sigma}_{11}(\boldsymbol{x},t) \\ \dot{\sigma}_{22}(\boldsymbol{x},t) \\ \dot{\sigma}_{33}(\boldsymbol{x},t) \\ \dot{\sigma}_{23}(\boldsymbol{x},t) \\ \dot{\sigma}_{13}(\boldsymbol{x},t) \\ \dot{\sigma}_{12}(\boldsymbol{x},t) \end{pmatrix} \mathrm{d}V = \int_S \begin{pmatrix} v_1(\boldsymbol{x},t)n_1 \\ v_2(\boldsymbol{x},t)n_2 \\ v_3(\boldsymbol{x},t)n_3 \\ v_2(\boldsymbol{x},t)n_3 + v_3(\boldsymbol{x},t)n_2 \\ v_1(\boldsymbol{x},t)n_3 + v_3(\boldsymbol{x},t)n_1 \\ v_1(\boldsymbol{x},t)n_2 + v_2(\boldsymbol{x},t)n_1 \end{pmatrix} \mathrm{d}S \tag{4.3}$$

The equation of motion (4.1) together with the deformation rate equation (4.3) describe the evolution of the set of variables $\{v_i, \sigma_{ij}\}$ in time and space and constitute the fundamental equations for the numerical approach[1]. The inhomogeneity of the problem has been explicitly indicated in the material variables $\rho(\boldsymbol{x})$ and $\boldsymbol{s}(\boldsymbol{x})$.

The discretization of the problem involves two steps. In the first step, the material parameters must be discretized on a material grid of cells $m^{(n)}$ with the material parameters being constant in each cell $m^{(n)}$

$$\boldsymbol{s}(\boldsymbol{x}) \to \boldsymbol{s}^{(n)}, \qquad \rho(\boldsymbol{x}) \to \rho^{(n)}$$

In the second step, the variables $\{v_i, \sigma_{ij}\}$ should be discretized on another grid $g^{(n)}$

$$v_i(\boldsymbol{x},t) \to v_i^{(n)}(t), \qquad \sigma_{ij}(\boldsymbol{x},t) \to \sigma_{ij}^{(n)}(t)$$

The two grids must then be positioned relative to each other, such that certain boundary conditions are satisfied. This is described below.

With respect to a coordinate system $\{\boldsymbol{e}_1, \boldsymbol{e}_2, \boldsymbol{e}_3\}$, a material grid consisting of cubic cells with an elastic matrix and a mass density specified for each cell is considered. The edge lengths of a cell are Δx such that the volume of a cell is $V = (\Delta x)^3$ and the surface area of a single face is $S = (\Delta x)^2$. The faces of the cells have normal vectors parallel to the coordinate axes. The geometry of the material cell $m^{(n)}$ is shown in Fig. 4.1.

The relative positions of the discretized components $v_i^{(n)}(t)$ and $\sigma_{ij}^{(n)}(t)$ are determined through the approximation of the integrals in (4.1) and (4.3) as follows. For each $v_i^{(n)}$ component, the volume of integration in (4.1) is a cubic cell centered at the $v_i^{(n)}$ component and with edge lengths Δx. The component is assumed constant within the volume of integration. The surface integral in (4.1) requires appropriate stress components to be defined at the faces of the integration volume. The involved stress components are assumed constant on each face. For a $\sigma_{ij}^{(n)}$ component, the volume of integration in (4.3) is again a cubic cell centered at the $\sigma_{ij}^{(n)}$ component, with the component assumed constant within the volume of integration. The surface integral in (4.3) requires components $v_i^{(n)}$ to be defined at the faces of the volume of integration. Each component $v_i^{(n)}$ is again assumed constant on the faces. This defines the positions of the components relative to each other. When placing the two grids relative to a each other, care must be taken that the boundary conditions (3.13) are satisfied. The final result is shown in Fig. 4.1 in the case of an isotropic material. As will be shown later, interpolations from the v_i components must be made in the anisotropic case.

[1]The two integral equations together with their discretization justifies the name abbreviated EFIT.

It turns out [47], that the diagonal stress components $\sigma_{ii}^{(n)}$ are positioned at the center of material cell $m^{(n)}$, while the off-diagonal stress components $\sigma_{ij}^{(n)}$, $i \neq j$ are placed at the edges of the cell. The $v_i^{(n)}$ components are placed at the face centers with the corresponding normal vectors $\boldsymbol{e}_i$. It is seen that the off-diagonal stress components are continuous across the correct material cell surfaces. As an example, a material cell surface could not be placed through the point containing the three diagonal stress components since this would impose unreal restrictions on two of the components.

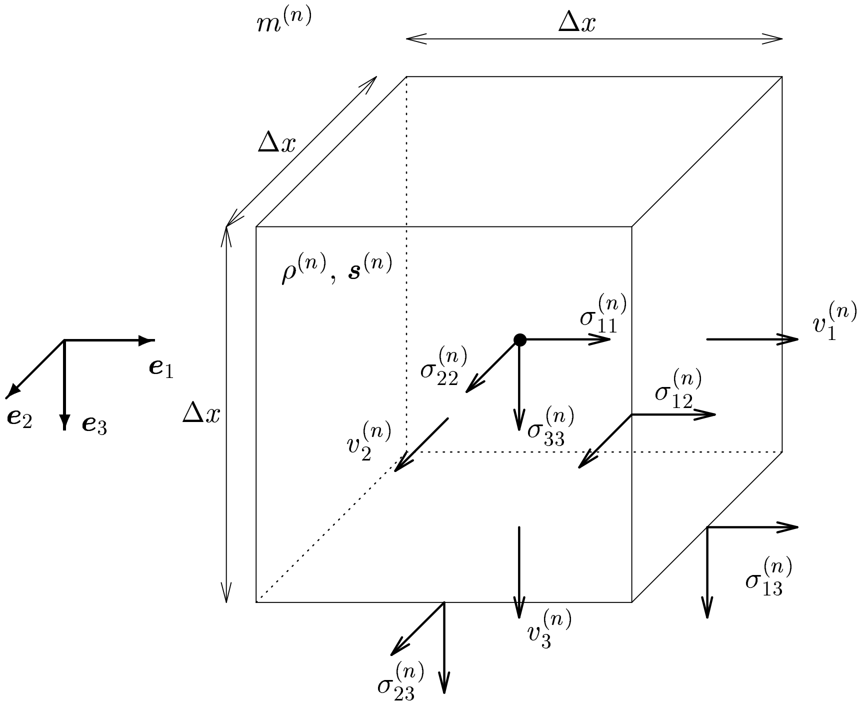

Figure 4.1: Material cell $m^{(n)}$ together with the associated components $v_i^{(n)}, \sigma_{ij}^{(n)}$ showing their relative positions.

For a given material cell $m^{(n)}$ we may consider the neighbouring cells. The neighbouring cell along the $\boldsymbol{e}_1$ axis is denoted $n + M_1$ (with a minus in the negative direction). Likewise the neighbouring cells along the axes $\boldsymbol{e}_2$ and $\boldsymbol{e}_3$ are denoted $n + M_2$ and $n + M_3$ respectively. With these definitions in mind, the difference equations together with examples of their derivations are given in the following two subsections.

4.2 Spatial discretization of the v_i components

The derivation of the equation for $v_1^{(n)}$ from (4.1) is shown in the following. As mentioned above, the volume of integration $I_{v_1}^{(n)}$ is a cubic cell centered at $v_1^{(n)}$ and with edge lengths Δx. The situation is illustrated in Fig. 4.2, where it is seen that the integration volume involves the two material cells $m^{(n)}$ and $m^{(n+M_1)}$. From (4.1) we thus get

$$\dot{v}_1^{(n)}(t)\frac{\rho^{(n)}+\rho^{(n+M_1)}}{2}(\Delta x)^3 =$$
$$\left(\sigma_{11}^{(n+M_1)}(t)-\sigma_{11}^{(n)}(t)+\sigma_{12}^{(n)}(t)-\sigma_{12}^{(n-M_2)}(t)+\sigma_{13}^{(n)}(t)-\sigma_{13}^{(n-M_3)}(t)\right)(\Delta x)^2$$

resulting in

$$\dot{v}_1^{(n)}(t)=\frac{1}{\Delta x}\frac{2}{\rho^{(n)}+\rho^{(n+M_1)}}\times$$
$$\left(\sigma_{11}^{(n+M_1)}(t)-\sigma_{11}^{(n)}(t)+\sigma_{12}^{(n)}(t)-\sigma_{12}^{(n-M_2)}(t)+\sigma_{13}^{(n)}(t)-\sigma_{11}^{(n-M_3)}(t)\right) \tag{4.4}$$

In a similar way we may obtain the equations for the two other components

$$\dot{v}_2^{(n)}(t)=\frac{1}{\Delta x}\frac{2}{\rho^{(n)}+\rho^{(n+M_2)}}\times$$
$$\left(\sigma_{12}^{(n)}(t)-\sigma_{12}^{(n-M_1)}(t)+\sigma_{22}^{(n+M_2)}(t)-\sigma_{22}^{(n)}(t)+\sigma_{23}^{(n)}(t)-\sigma_{23}^{(n-M_3)}(t)\right) \tag{4.5}$$

and

$$\dot{v}_3^{(n)}(t)=\frac{1}{\Delta x}\frac{2}{\rho^{(n)}+\rho^{(n+M_3)}}\times$$
$$\left(\sigma_{13}^{(n)}(t)-\sigma_{13}^{(n-M_1)}(t)+\sigma_{23}^{(n)}(t)-\sigma_{23}^{(n-M_2)}(t)+\sigma_{33}^{(n+M_3)}(t)-\sigma_{33}^{(n)}(t)\right) \tag{4.6}$$

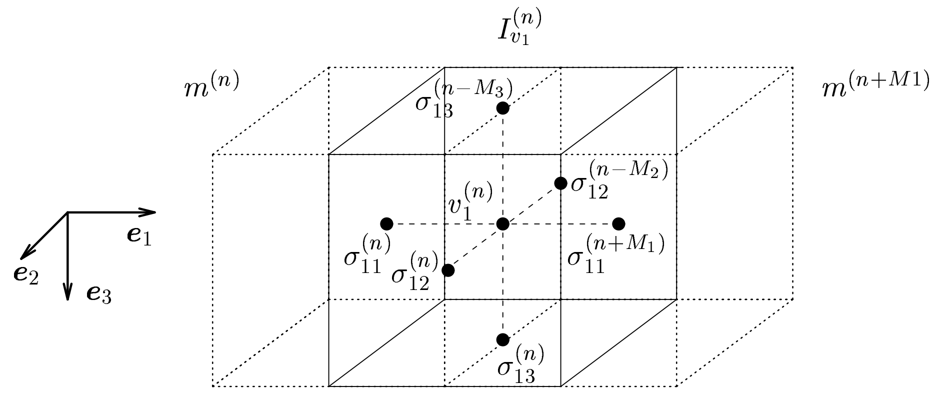

Figure 4.2: Volume of integration $I_{v_1}^{(n)}$ for the $v_1^{(n)}$ component together with the required stress components. Material parameters from two different material cells $m^{(n)}$ and $m^{(n+M_1)}$ are involved.

4.3 Spatial discretization of the σ_{ij} components

The equations for the stress components follow from the deformation rate equation (4.3). As above, the integration volume is a cubic cell centered at the $\sigma_{ij}^{(n)}$ component in question.

It is then clear that a distinction must be made between the diagonal and the off-diagonal stress components. The volume of integration for the former involves only one material cell while for the latter it involves four cells.

The situation is illustrated in Fig. 4.3 for the $\sigma_{ii}^{(n)}$ components, where the volume of integration $I_{\sigma_{ii}}^{(n)}$ coincides with material cell $m^{(n)}$. For the volume of integration in question it is convenient to introduce local coordinates for the v_i components. With reference to Fig. 4.3, components positioned at the front face (positive $\boldsymbol{e}_2$) are labeled with an (f) as superscript. Likewise, the following notation is used for the other faces: back (b), right (r), left (l), up (u) and down (d). As indicated with a bar, additional $\bar{v}_i$ are required at the faces of $I_{\sigma_{ii}}^{(n)}$ relative to the isotropic situation. The equation for the diagonal stress components becomes (with the irrelevant off-diagonal stress components indicated by a dot $\cdot$)

$$\begin{pmatrix} \dot{\sigma}_{11}^{(n)}(t) \\ \dot{\sigma}_{22}^{(n)}(t) \\ \dot{\sigma}_{33}^{(n)}(t) \\ \cdot \\ \cdot \\ \cdot \end{pmatrix} (\Delta x)^3 = \boldsymbol{c}^{(n)} \begin{pmatrix} v_1^{(r)}(t) - v_1^{(l)}(t) \\ v_2^{(f)}(t) - v_2^{(b)}(t) \\ v_3^{(d)}(t) - v_3^{(u)}(t) \\ \bar{v}_2^{(d)}(t) - \bar{v}_2^{(u)}(t) + \bar{v}_3^{(f)}(t) - \bar{v}_3^{(b)}(t) \\ \bar{v}_1^{(d)}(t) - \bar{v}_1^{(u)}(t) + \bar{v}_3^{(r)}(t) - \bar{v}_3^{(l)}(t) \\ \bar{v}_1^{(f)}(t) - \bar{v}_1^{(b)}(t) + \bar{v}_2^{(r)}(t) - \bar{v}_2^{(l)}(t) \end{pmatrix} (\Delta x)^2$$

where the equation has been multiplied with the elastic matrix $\boldsymbol{c}^{(n)}$ (being the normal matrix inverse of $\boldsymbol{s}^{(n)}$) on both sides. Written out for each diagonal component (no summation over i), we have

$$\begin{aligned} \dot{\sigma}_{ii}^{(n)}(t) \quad = \quad & \frac{1}{\Delta x} \Big[c_{i1}^{(n)} \left(v_1^{(r)}(t) - v_1^{(l)}(t) \right) + \\ & c_{i2}^{(n)} \left(v_2^{(f)}(t) - v_2^{(b)}(t) \right) + \\ & c_{i3}^{(n)} \left(v_3^{(d)}(t) - v_3^{(u)}(t) \right) + \\ & c_{i4}^{(n)} \left(\bar{v}_2^{(d)}(t) - \bar{v}_2^{(u)}(t) + \bar{v}_3^{(f)}(t) - \bar{v}_3^{(b)}(t) \right) + \\ & c_{i5}^{(n)} \left(\bar{v}_1^{(d)}(t) - \bar{v}_1^{(u)}(t) + \bar{v}_3^{(r)}(t) - \bar{v}_3^{(l)}(t) \right) + \\ & c_{i6}^{(n)} \left(\bar{v}_1^{(f)}(t) - \bar{v}_1^{(b)}(t) + \bar{v}_2^{(r)}(t) - \bar{v}_2^{(l)}(t) \right) \Big], \qquad i = 1,2,3 \end{aligned} \tag{4.7}$$

In an implementation situation a transformation from local coordinates back to global coordinates should be performed. This is trivial and will not be done here. As seen, the additional components $\bar{v}_i$ stem from the last three terms on the righthand side. In anisotropic materials the three constants $c_{i4}^{(n)}$, $c_{i5}^{(n)}$, and $c_{i6}^{(n)}$ are in general non-zero as opposed to isotropic materials. These additional components are obtained as averages over the corresponding four nearest neighbours. For example

$$\bar{v}_1^{(f)} = \frac{1}{4} \left(v_1^{(n)} + v_1^{(n-M_1)} + v_1^{(n+M_2)} + v_1^{(n-M_1+M_2)} \right)$$

The off-diagonal stress components are situated at the edges of the material cells, see Fig. 4.1. Thus, as noted above, the volume of integration with center at one of

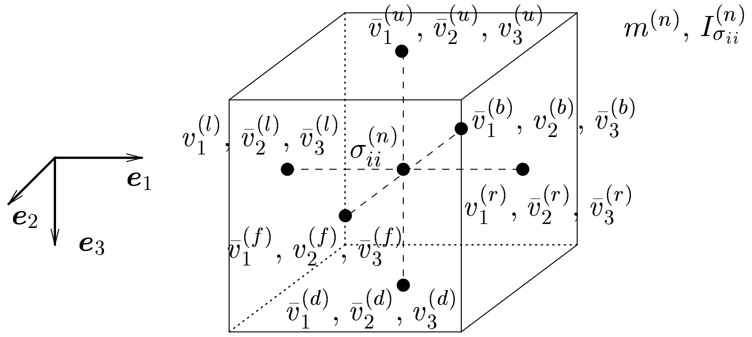

Figure 4.3: Volume of integration $I_{\sigma_{ii}}^{(n)}$ for the $\sigma_{ii}^{(n)}$ components.

these components involves four material cells. This is illustrated in Fig. 4.4 for the $\sigma_{13}^{(n)}$ component. In this case material cells $m^{(n)}$, $m^{(n+M_1)}$, $m^{(n+M_3)}$ and $m^{(n+M_1+M_3)}$ are included in the volume integral. Again, additional components $\bar{v}_i$ are needed at each cube face in the integration. The result for the $\sigma_{13}^{(n)}$ component is (with irrelevant stress components indicated by a dot $\cdot$)

$$\begin{pmatrix} \cdot \\ \cdot \\ \cdot \\ \cdot \\ \dot{\sigma}_{13}^{(n)}(t) \\ \cdot \end{pmatrix} = \frac{\bar{\boldsymbol{c}}_{13}^{(n)}}{\Delta x} \begin{pmatrix} \bar{v}_1^{(r)}(t) - \bar{v}_1^{(l)}(t) \\ \bar{v}_2^{(f)}(t) - \bar{v}_2^{(b)}(t) \\ \bar{v}_3^{(d)}(t) - \bar{v}_2^{(u)}(t) \\ \bar{v}_2^{(d)}(t) - \bar{v}_2^{(u)}(t) + \bar{v}_3^{(f)}(t) - \bar{v}_3^{(b)}(t) \\ v_1^{(d)}(t) - v_1^{(u)}(t) + v_3^{(r)}(t) - v_3^{(l)}(t) \\ \bar{v}_1^{(f)}(t) - \bar{v}_1^{(b)}(t) + \bar{v}_2^{(r)}(t) - \bar{v}_2^{(l)}(t) \end{pmatrix}$$

where an elastic matrix $\bar{\boldsymbol{c}}_{13}^{(n)}$ "averaged" over the four involved material cells has been introduced as

$$\bar{\boldsymbol{s}}_{13}^{(n)} = \frac{1}{4}(\boldsymbol{s}^{(n)} + \boldsymbol{s}^{(n+M_1)} + \boldsymbol{s}^{(n+M_3)} + \boldsymbol{s}^{(n+M_1+M_3)}) \tag{4.8}$$

$$\bar{\boldsymbol{c}}_{13}^{(n)} = \left(\bar{\boldsymbol{s}}_{13}^{(n)}\right)^{-1} \tag{4.9}$$

Extraction of the fifth equation governing $\dot{\sigma}_{13}^{(n)}(t)$ results in (here, a comma in the matrix subscript does not imply differentiation)

$$\begin{aligned} \dot{\sigma}_{13}^{(n)}(t) = \frac{1}{\Delta x} \Big[& \bar{c}_{13,51}^{(n)} \left(\bar{v}_1^{(r)}(t) - \bar{v}_1^{(l)}(t)\right) + \\ & \bar{c}_{13,52}^{(n)} \left(\bar{v}_2^{(f)}(t) - \bar{v}_2^{(b)}(t)\right) + \\ & \bar{c}_{13,53}^{(n)} \left(\bar{v}_3^{(d)}(t) - \bar{v}_3^{(u)}(t)\right) + \\ & \bar{c}_{13,54}^{(n)} \left(\bar{v}_2^{(d)}(t) - \bar{v}_2^{(u)}(t) + \bar{v}_3^{(f)}(t) - \bar{v}_3^{(b)}(t)\right) + \\ & \bar{c}_{13,55}^{(n)} \left(v_1^{(d)}(t) - v_1^{(u)}(t) + v_3^{(r)}(t) - v_3^{(l)}(t)\right) + \\ & \bar{c}_{13,56}^{(n)} \left(\bar{v}_1^{(f)}(t) - \bar{v}_1^{(b)}(t) + \bar{v}_2^{(r)}(t) - \bar{v}_2^{(l)}(t)\right)\Big] \end{aligned} \tag{4.10}$$

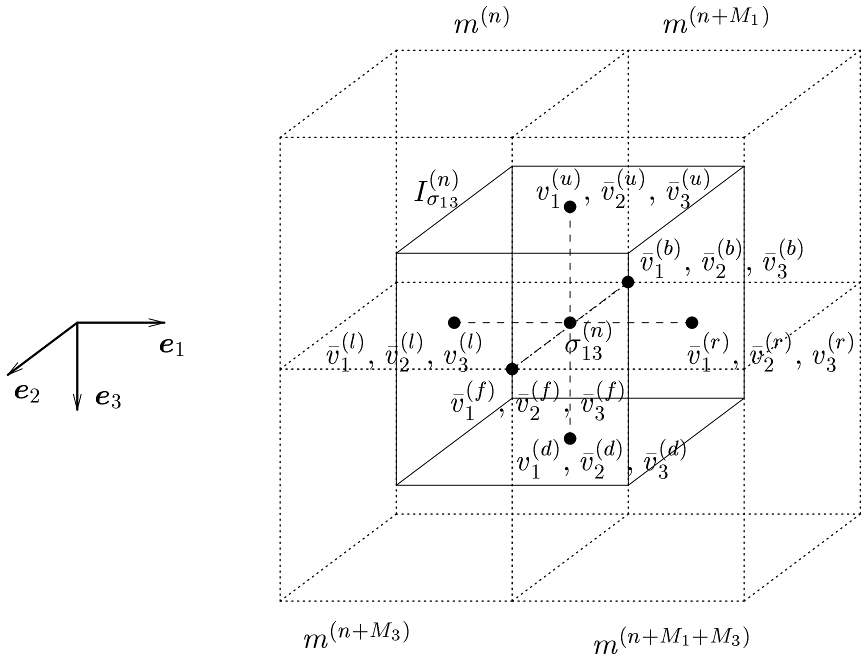

Figure 4.4: Volume of integration (solid lines) $I_{\sigma_{13}}^{(n)}$ for the σ_{13} component. Dotted lines indicate the four material cells $m^{(n)}$, $m^{(n+M_1)}$, $m^{(n+M_3)}$ and $m^{(n+M_1+M_3)}$.

It should be noted that the averages in (4.10) are different from those occurring for the $I_{\sigma_{ii}}^{(n)}$ volume in (4.7). For example, as opposed to the previous case, here we have

$$\bar{v}_1^{(f)} = \frac{1}{4}\left(\bar{v}_1^{(n)} + \bar{v}_1^{(n+M_3)} + \bar{v}_1^{(n+M_2)} + \bar{v}_1^{(n+M_2+M_3)}\right)$$

In a similar way, we may define "averaged" elastic matrices

$$\bar{\boldsymbol{s}}_{23}^{(n)} = \frac{1}{4}(\boldsymbol{s}^{(n)} + \boldsymbol{s}^{(n+M_2)} + \boldsymbol{s}^{(n+M_3)} + \boldsymbol{s}^{(n+M_2+M_3)}) \tag{4.11}$$

$$\bar{\boldsymbol{c}}_{23}^{(n)} = \left(\bar{\boldsymbol{s}}_{23}^{(n)}\right)^{-1} \tag{4.12}$$

and

$$\bar{\boldsymbol{s}}_{12}^{(n)} = \frac{1}{4}(\boldsymbol{s}^{(n)} + \boldsymbol{s}^{(n+M_1)} + \boldsymbol{s}^{(n+M_2)} + \boldsymbol{s}^{(n+M_1+M_2)}) \tag{4.13}$$

$$\bar{\boldsymbol{c}}_{12}^{(n)} = \left(\bar{\boldsymbol{s}}_{12}^{(n)}\right)^{-1} \tag{4.14}$$

in order to obtain equations for the two other stress components. Since the volumes of integration are simply translated, the new equations, apart from using different averaged elastic matrices, differ only in the places where the components are averages. We have

$$\begin{aligned}
\dot{\sigma}_{23}^{(n)}(t) \quad = \quad & \frac{1}{\Delta x}\Big[\bar{c}_{23,41}^{(n)}\left(\bar{v}_1^{(r)}(t)-\bar{v}_1^{(l)}(t)\right)+ \\
& \bar{c}_{23,42}^{(n)}\left(\bar{v}_2^{(f)}(t)-\bar{v}_2^{(b)}(t)\right)+ \\
& \bar{c}_{23,43}^{(n)}\left(\bar{v}_3^{(d)}(t)-\bar{v}_3^{(u)}(t)\right)+ \\
& \bar{c}_{23,44}^{(n)}\left(v_2^{(d)}(t)-v_2^{(u)}(t)+v_3^{(f)}(t)-v_3^{(b)}(t)\right)+ \\
& \bar{c}_{23,45}^{(n)}\left(\bar{v}_1^{(d)}(t)-\bar{v}_1^{(u)}(t)+\bar{v}_3^{(r)}(t)-\bar{v}_3^{(l)}(t)\right)+ \\
& \bar{c}_{23,46}^{(n)}\left(\bar{v}_1^{(f)}(t)-\bar{v}_1^{(b)}(t)+\bar{v}_2^{(r)}(t)-\bar{v}_2^{(l)}(t)\right)\Big]
\end{aligned} \tag{4.15}$$

and

$$\begin{aligned}
\dot{\sigma}_{12}^{(n)}(t) \quad = \quad & \frac{1}{\Delta x}\Big[\bar{c}_{12,61}^{(n)}\left(\bar{v}_1^{(r)}(t)-\bar{v}_1^{(l)}(t)\right)+ \\
& \bar{c}_{12,62}^{(n)}\left(\bar{v}_2^{(f)}(t)-\bar{v}_2^{(b)}(t)\right)+ \\
& \bar{c}_{12,63}^{(n)}\left(\bar{v}_3^{(d)}(t)-\bar{v}_3^{(u)}(t)\right)+ \\
& \bar{c}_{12,64}^{(n)}\left(\bar{v}_2^{(d)}(t)-\bar{v}_2^{(u)}(t)+\bar{v}_3^{(f)}(t)-\bar{v}_3^{(b)}(t)\right)+ \\
& \bar{c}_{12,65}^{(n)}\left(\bar{v}_1^{(d)}(t)-\bar{v}_1^{(u)}(t)+\bar{v}_3^{(r)}(t)-\bar{v}_3^{(l)}(t)\right)+ \\
& \bar{c}_{12,66}^{(n)}\left(v_1^{(f)}(t)-v_1^{(b)}(t)+v_2^{(r)}(t)-v_2^{(l)}(t)\right)\Big]
\end{aligned} \tag{4.16}$$

In Fig. 4.5 an example of a grid with cell numbers 1 to 84 is shown in 2D where a slice has been cut through the x_1x_3-plane. For computational reasons, we shall be exclusively concerned with the 2D case in the remaining part of the thesis. The material boundary is shown with thick lines. As seen, a dummy layer has been added around the material. The dummy layer is suitable for modelling transducer actions on the material surface. Integration volumes $I_{v_1}^{(33)}$ and $I_{v_3}^{(46)}$ for the variables $v_1^{(33)}$ and $v_3^{(46)}$ respectively are shown together with the integration volume $I_{\sigma_{13}}^{(14)}$ for $\sigma_{13}^{(14)}$. As seen, the variables $v_3^{(5)}$ and $v_1^{(37)}$ are positioned at the boundary. Such boundary variables are calculated using half integration volumes as indicated. This is the subject of section 4.7.

4.4 Temporal discretization of the components

In the previous two sections, the variables were discretized in space and the corresponding equations were derived. Here, the same process will be carried out for the time dimension. To this end we consider the following basic equations

$$v_i(t) = v_i(t_0) + \int_{t_0}^{t} \dot{v}_i(t')\,\mathrm{d}t' \tag{4.17}$$

and

$$\sigma_{ij}(t) = \sigma_{ij}(t_0) + \int_{t_0}^{t} \dot{\sigma}_{ij}(t')\,\mathrm{d}t' \tag{4.18}$$

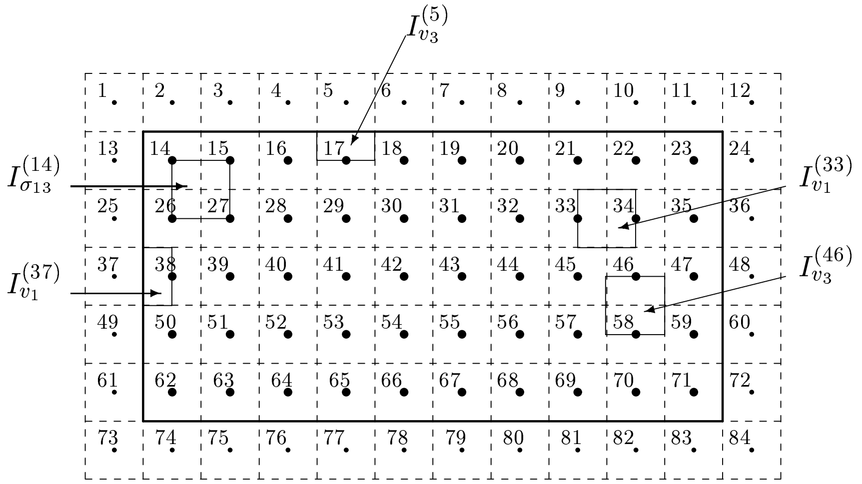

Figure 4.5: Example of grid in 2D.

We discretize the time in intervals of Δt. For the v_i components, the time points become $0, \ldots, (z-1)\Delta t, z\,\Delta t, \ldots$ for integer z. For the σ_{ij} components, the time points are displaced by half the interval, such that the time points become $\frac{1}{2}\Delta t, \ldots, (z-\frac{1}{2})\Delta t, (z+\frac{1}{2})\Delta t, \ldots$. Applying the midpoint rule in the evaluation of the above integrals between two neighbouring time points, we get (suppressing the space variables)

$$v_i^{(z)} = v_i^{(z-1)} + \dot{v}_i^{(z-\frac{1}{2})}\Delta t \tag{4.19}$$

and

$$\sigma_{ij}^{(z+\frac{1}{2})} = \sigma_{ij}^{(z-\frac{1}{2})} + \dot{\sigma}_{ij}^{(z)}\Delta t \tag{4.20}$$

with $\dot{v}_i^{(z-\frac{1}{2})}$ given by (4.4), (4.5), (4.6) and $\dot{\sigma}_{ij}^{(z)}$ by (4.7), (4.10), (4.15) and (4.16). It is immediately seen, that the method is explixit in time. That is, variables at different time steps are separated on each side of the equation. Thus, as opposed to an implicit method, it is not necessary to solve a set of linear equations. This is computationally very attractive.

The numerical method presented above based on the integral equations (4.1) and (4.2) is of course just an alternative to solving the equivalent differential equations (2.12). For homogeneous (isotropic) materials the above obtained equations are identical to the ones obtained in [69, 70] directly by solving the differential equations as was noted in section 2.6. It is in the case when the material becomes inhomogeneous, that the set of integral equations provides a more natural framework.

4.5 Accuracy of discretization

A word on the error of the introduced approximations in the previous two sections is in order here. The integrand in the volume and surface integrals in space has been approximated by it's value at the center. Using the Taylor expansion of the indefinite integral to a function f, the error introduced can be evaluated for a line -, surface - and volume integral as follows

$$
\begin{aligned}
\frac{1}{\Delta x}\int_{x_0}^{x_0+\Delta x} f(x,y_0,z_0)\,\mathrm{d}x &= f(x_0+\frac{\Delta x}{2},y_0,z_0)+\mathcal{O}\left((\Delta x)^2\right)\\
\frac{1}{(\Delta x)^2}\int_{y_0}^{y_0+\Delta x}\int_{x_0}^{x_0+\Delta x} f(x,y,z_0)\,\mathrm{d}x\,\mathrm{d}y &= f(x_0+\frac{\Delta x}{2},y_0+\frac{\Delta x}{2},z_0)+\mathcal{O}\left((\Delta x)^2\right)\\
\frac{1}{(\Delta x)^3}\int_{z_0}^{z_0+\Delta x}\int_{y_0}^{y_0+\Delta x}\int_{x_0}^{x_0+\Delta x} f(x,y,z)\,\mathrm{d}x\,\mathrm{d}y\,\mathrm{d}z &= f(x_0+\frac{\Delta x}{2},y_0+\frac{\Delta x}{2},z_0+\frac{\Delta x}{2})\\
&\quad+\mathcal{O}\left((\Delta x)^2\right)
\end{aligned}
$$

Each equation has been divided by the integration interval (area or volume) in order to make the error on the right hand side independent of this. In all three cases, the error is then seen to be of second order. According to (4.1) and (4.2), volume - and surface integrals enter the fundamental equations. As both integrals according to the above are evaluated to second order, the numerical approach is of second order in space.

From this discussion and (4.19-4.20), it is immediately seen that the numerical approach is of second order in time as well.

4.6 Stability of the numerical method

A detailed von Neumann analysis based on monochromatic plane waves of the stability of the numerical method has been carried out in [23,47] and will not be repeated here.

For unbounded homogeneous, isotropic media, the stability is ensured provided that the following (Courant-Friedrichs-Lewy) criterium in 3D is fulfilled

$$\Delta t \le \frac{1}{c_l}\frac{\Delta x}{\sqrt{3}} \tag{4.21}$$

and in 2D

$$\Delta t \le \frac{1}{c_l}\frac{\Delta x}{\sqrt{2}} \tag{4.22}$$

where c_l is the longitudinal phase velocity. If the medium is inhomogeneous, then c_l should be replaced with the largest phase velocity $c_{l,max}$ occurring in the medium. If the medium is anisotropic then the above phase velocities are replaced with the corresponding group velocities.

Furthermore it is mentioned, that consistency of the method is proved in the above references. This implies that the discrete dispersion relation has the continuous dispersion relation as a limit. In a practical sense, this means that numerical dispersion effects can be avoided by using a fine enough space grid. As a final point, the method is shown to be non-dissipative in the references.

The choice of Δx in an actual simulation is mainly a matter of experience. As noted above numerical dispersion may be avoided by making Δx small enough relative to the involved wavelengths. In this thesis, good results have been obtained using $\Delta x \sim \frac{\lambda}{10}$, where λ is the smallest occurring wavelength in the medium. For frequencies of a few MHz, a typical value is $\Delta x \approx 0.1\,\mathrm{mm}$.

4.7 Boundary conditions

The effect of internal boundaries in the medium in the sense of changes in the material parameters is automatically handled by the numerical method as it has been developed for inhomogeneous materials. However, explicit boundary conditions such as stress free boundaries, internal as well as external, must explicitly be incorporated into the algorithm. As a continuation of the discussion in section 2.3 of NDT scenarios typically involving stress free material boundaries, we shall restrict ourselves to this type of explicit boundary conditions.

The situation for the $v_3^{(n)}$ component is shown in Fig. 4.6. Two different cases must be considered. In the first case, $m^{(n)}$ is a vacuum cell with $v_3^{(n)}$ situated at the boundary and with $m^{(n+M_3)}$ being a material cell (left figure). This is the typical case on the upper side of the medium, see Fig. 4.5 with the variable $v_3^{(5)}$ and integration volume $I_{v_3}^{(5)}$. In the other case, $m^{(n)}$ is a material cell, again with $v_3^{(n)}$ situated at the boundary and $m^{(n+M_3)}$ being a vacuum cell (right figure). This is the typical case on the lower edge of the medium. As indicated in both figures, only half of the usual volume of integration (solid lines) is used in this boundary situation, namely that half located in the material cell.

For the first case, (4.1) thus becomes

$$\begin{aligned}\rho^{(n+M_3)}\dot{v}_3^{(n)}(t)\frac{(\Delta x)^3}{2} &= \left[\sigma_{13}^{(n)}(t)-\sigma_{13}^{(n-M_1)}(t)\right]\frac{(\Delta x)^2}{2}+\left[\sigma_{23}^{(n)}(t)-\sigma_{23}^{(n-M_2)}(t)\right]\frac{(\Delta x)^2}{2}+\\ &\quad\left[\sigma_{33}^{(n+M_3)}(t)-\sigma_{33}^{(m)}(t)\right](\Delta x)^2\end{aligned}$$

resulting in

$$\begin{aligned}\dot{v}_3^{(n)}(t) &= \frac{1}{\rho^{(n+M_3)}\Delta x}\left[\sigma_{13}^{(n)}(t)-\sigma_{13}^{(n-M_1)}(t)+\sigma_{23}^{(n)}(t)-\sigma_{23}^{(n-M_2)}(t)+\right.\\ &\quad\left.2\left(\sigma_{33}^{(n+M_3)}(t)-\sigma_{33}^{(m)}(t)\right)\right]\end{aligned}\tag{4.23}$$

For the second case

$$\begin{aligned}\dot{v}_3^{(n)}(t) &= \frac{1}{\rho^{(n)}\Delta x}\left[\sigma_{13}^{(n)}(t)-\sigma_{13}^{(n-M_1)}(t)+\sigma_{23}^{(n)}(t)-\sigma_{23}^{(n-M_2)}(t)+\right.\\ &\quad\left.2\left(\sigma_{33}^{(m)}(t)-\sigma_{33}^{(n)}(t)\right)\right]\end{aligned}\tag{4.24}$$

In a similar way, equations for the two other components $\dot{v}_1$ and $\dot{v}_2$ may be obtained. As seen in Fig. 4.6, as well as in (4.23) and (4.24) an imaginary variable $\sigma_{33}^{(m)}$ has been introduced. If the boundary is stress free, we have $\sigma_{33}^{(m)} = \sigma_{23}^{(n)} = \sigma_{23}^{(n-M_2)} = \sigma_{13}^{(n)} = \sigma_{13}^{(n-M_1)} = 0$. However, different types of transducers may be modelled by specifying their time dependence through these variables, which is the reason for retaining them in the above equations. An element of a typical piezoelectric transducer may be modelled by specifying $\sigma_{33}^{(m)}(t)$, while a SH transducer may be modelled by specifying $\sigma_{23}^{(n)}(t)$.

Finally, a note on the accuracy of the components calculated at the boundary. In the case of the $v_3^{(n)}$ component, the integrand is evaluated at one of the end points in the integral over x_3. Thus, following the previous general notation for one of the integrals

$$\frac{1}{\Delta x}\int_{x_0}^{x_0+\frac{\Delta x}{2}} f(x,y_0,z_0)\,\mathrm{d}x = f(x_0,y_0,z_0)+\mathcal{O}(\Delta x)$$

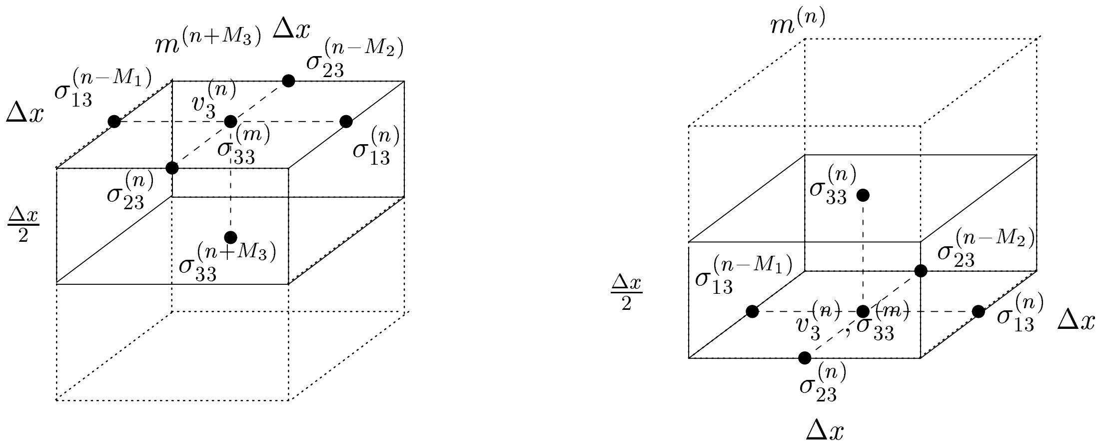

Figure 4.6: Volume of integrations for the $\dot{v}_3^{(n)}$ component at a boundary. Left: $m^{(n)}$ is a vacuum cell and $m^{(n+M_3)}$ is a material cell. Right: The reversed situation.

That is, in this case the error is of first order. The evaluation of the two other integrals is identical to the one shown for the full volume of integration. From this, it is concluded that the algorithm is of first order at the boundary. Unfortunately this may mean that the algorithm globally is of first order in space. Apart from the comparison with the analytical method in the previous chapter, the implications of this have not been investigated further here. In [47], however, a higher order algorithm is presented.

4.8 Pulse signal of the transducer

When modelling a transducer at the surface of the material, it is necessary to specify the time dependence or pulse signal of the transducer action on the material. Examples of pulse signals have already been met in section 2.6 as well as in section 3.2 (although the latter was a rather idealistic pulse as noted). In connection with the numerical method presented here, the following raised cosine function is considered as pulse signal

$$f(t;n) = \begin{cases} \frac{(-1)^2}{2}\left[1-\cos\left(\frac{\omega_0}{n}t\right)\right]\cos(\omega_0 t), & 0 < t < n\frac{2\pi}{\omega_0} \\ 0, & \text{else} \end{cases} \tag{4.25}$$

where n is a positive integer used to control the sharpness of the pulse. This function has also been considered in [45,47]. The corresponding frequency spectrum may be found analytically as

$$\tilde{f}(\omega;n) = \frac{(-1)^{n+1}}{2}\sin\left(\frac{n\pi}{\omega_0}\omega\right)\left[\frac{\omega}{\omega^2-(\frac{n-1}{n})^2\omega_0^2} - \frac{2\omega}{\omega^2-\omega_0^2} + \frac{\omega}{\omega^2-(\frac{n+1}{n})^2\omega_0^2}\right]\mathrm{e}^{\mathrm{i}\frac{n\pi}{\omega_0}\omega} \tag{4.26}$$

Examples of graphs are shown in Fig. 4.7 for the time domain and in Fig. 4.8 for the frequency domain (symmetric about the y-axis) for $n = 2$ and $n = 5$. Clearly, the frequency spectrum becomes narrower for increasing n. As seen, there is a large resemblance with the pulse signals shown in Fig. 2.3 with the main difference being the compact support of (4.25) in the time domain.

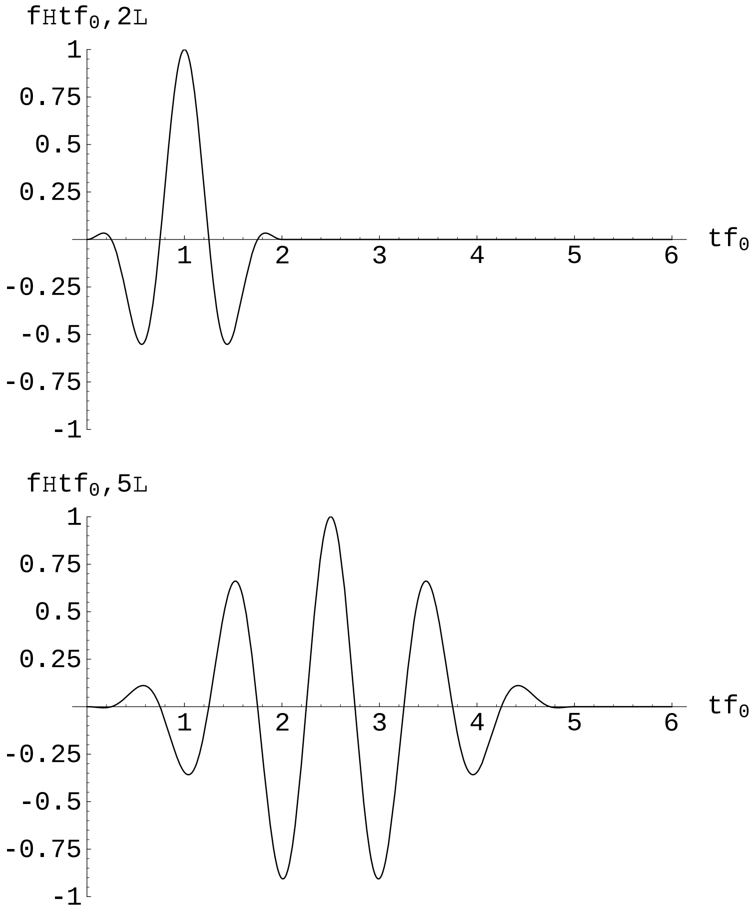

Figure 4.7: Pulse shapes in the time domain for $f(tf_0;n)$ with $n = 2$ (upper) and $n = 5$ (lower).

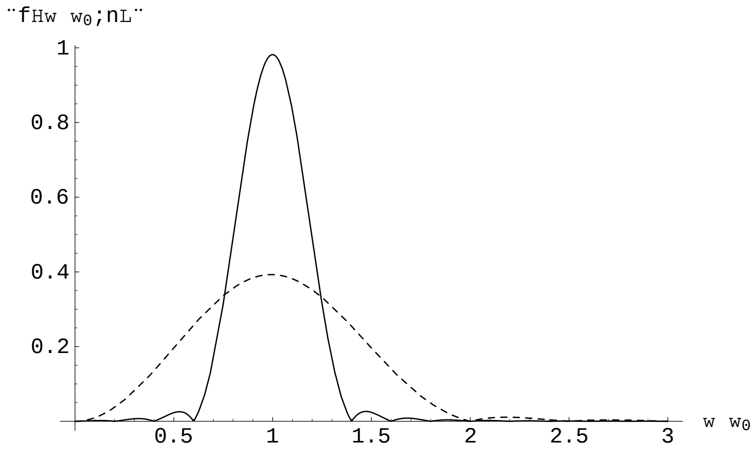

Figure 4.8: Frequency spectrum $|\tilde{f}(\omega/\omega_0;n)|$ for $n = 2$ (dashed line) and $n = 5$ (solid line).

Fig. 4.9 shows the pulse shape and frequency spectrum for a transducer from Panametrics with specifications given in the legend. Fig. 4.10 shows equivalent information for a transducer from RTD. The Panametrics transducer signal is modelled reasonably well by $f(t;2)$ (except for a change of sign) while the RTD transducer signal is reasonably well modelled by $f(t;5)$.

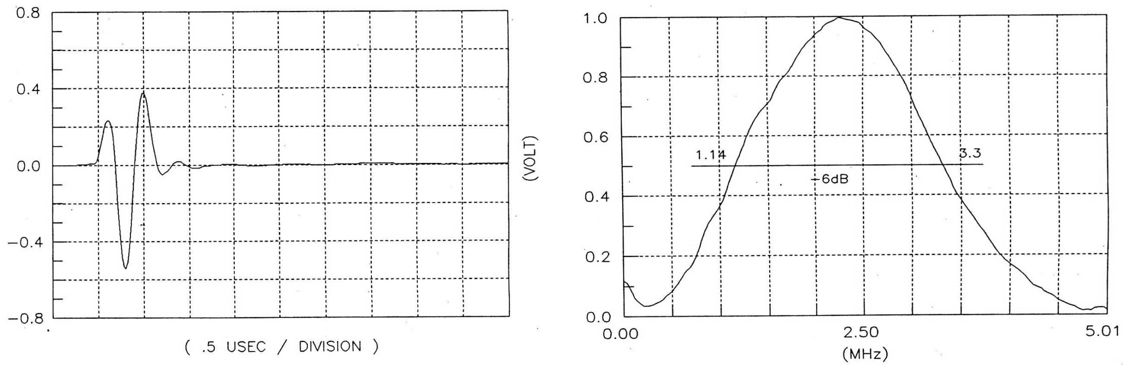

Figure 4.9: Transducer signal (left) and frequency spectrum (right) from a Panametrics 2 MHZ transducer. Center frequency is 2.22 MHz and peak frequency is 2.25 MHz. -6 dB bandwidth is 2.16 MHz (indicated on figure) or 97.30% of the center frequency.

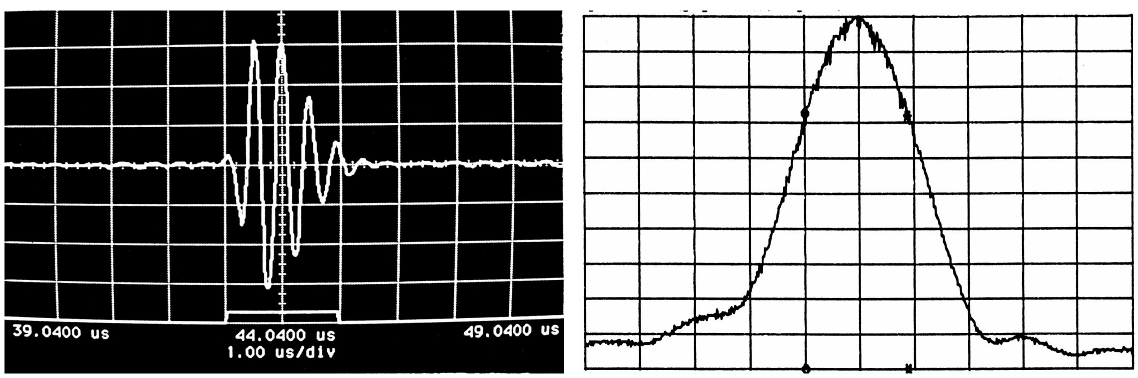

Figure 4.10: Transducer signal (left) and frequency spectrum (right) for a RTD 45° L, 2 MHz transducer. Center frequency is 2.11 MHz and -3 dB bandwidth is 0.56 MHz (indicated on figure).

4.9 A model of the transducer as transmitter

In this thesis, an actual model of the piezoelectric transducer itself will not be carried out as this may well be considered a topic of its own [47]. Instead, the problem is restricted to that of specifying a realistic mechanical traction vector right below the transducer as a transmitter. This approach is also considered in other works, e.g. [13,47]. As a first simple illustration, consider Fig. 4.11 showing a 0° transducer. Roughly described, the transducer consists of a piezoelectric element with a damping material (such as an epoxy resin) on the back side and a cover on the front side. As shown in the figure, the time needed for the sound field to propagate through the cover is denoted t_0. A liquid coupling is assumed between the transducer and the material for maximum contact. Due to this coupling only normal stress components may be transferred to the surface of the material. Thus, when modelling the transmitter it is a matter of specifying the normal stress components at the surface in a suitable way. For ease of illustration, we consider in the following the transducer to be positioned on the upper horizontal boundary, see Fig. 4.5, with an outward normal vector $\boldsymbol{n} = -\boldsymbol{e}_3$. The x_3 component is constant at the surface of contact and is suppressed in the following. First the continuous case is considered for outlining the principles. Then the results are adapted to the discrete case.

From the above considerations, the transducer exerts a stress on the upper surface of the material in the direction $\boldsymbol{q} = (0, 0, 1)$. At the surface of contact, the boundary condition in its general form becomes

$$\begin{pmatrix} \sigma_{13}(x_1, t) \\ \sigma_{23}(x_1, t) \\ \sigma_{33}(x_1, t) \end{pmatrix} = -T_0 \boldsymbol{q} W(x_1) f\left(t - t_{ret}(x_1)\right) 1_{[x_1^{min}, x_1^{max}]}(x_1) \tag{4.27}$$

where $1_{[a,b]}(x)$ is 1 for $x \in [a, b]$ and 0 else. x_1^{min} and x_1^{max} denote the leftmost and the rightmost points of the surface of contact respectively. T_0 is the amplitude, $W(x_1)$ is a spatial weight function across the surface of contact and $f(t)$ describes the time dependence. In this thesis, however, we shall set $W(x_1) = 1$. $t_{ret}(x_1)$ denotes a retarded time which includes the above mentioned time t_0, but which is most important when considering angled probes or phased arrays. Although not realistic for a piezoelectric transducer with fluid coupling, the general form of the boundary condition (4.27) also allows the mechanical traction vector from a SH transducer, such as an electromagnetic acoustic transducer (EMAT), to be modelled simply by setting $\boldsymbol{q} = (0, 1, 0)$.

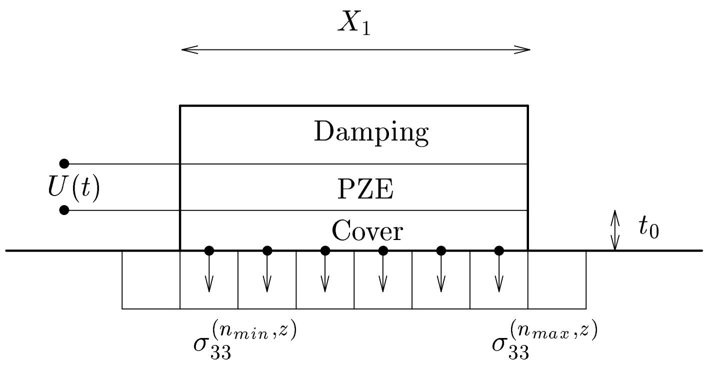

Figure 4.11: Model of transmitting 0° transducer.

Consider now an angled probe such as the one illustrated in Fig. 4.12. The longitudinal wave speed and incident angle in the transducer wedge (usually plexiglas with $v_p = 2730$m/s) are denoted by v_p and α_p respectively. The wave speed and the refracted angle in the reference material are denoted v_{ref} and α_{ref}. The point of refraction travels along the surface of contact with the speed v. From Snell's law, we have

$$\sin \alpha_p = \frac{v_p}{v_{ref}} \sin \alpha_{ref} \tag{4.28}$$

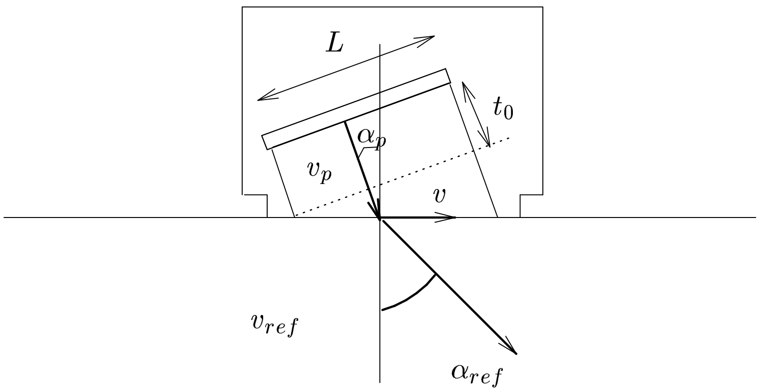

Figure 4.12: Angled probe

The speed of the point of refraction thus becomes

$$v = \frac{v_p}{\sin \alpha_p} = \frac{v_{ref}}{\sin \alpha_{ref}} \tag{4.29}$$

When modelling an angled probe, the retarded time is determined from this speed

$$t_{ret}(x_1) = t_0 + \frac{x_1 - x_1^{min}}{v_{ref}} \sin \alpha_{ref} \tag{4.30}$$

which is used in conjunction with (4.27). As an illustration, the reference material for the longitudinal 45° angled probe from RTD mentioned above is austenite with $v_l = 5750\frac{m}{s}$ and $v_t = 3150\frac{m}{s}$. The transducer wedge is of the above mentioned plexiglas. Thus, $\alpha_p = \arcsin(0.4747 \sin 45°) \approx 20°$. Furthermore, $v = 5750\frac{m}{s}/\sin 45° \approx 4066\frac{m}{s}$. From Snell's law, the angle of refraction for the transverse wave becomes $\arcsin(0.5478 \sin 45°) \approx 23°$. The 0° transducer is of course just a special case with $\alpha_{ref} = 0°$ in (4.30). In this thesis, we shall set $t_0 = 0$.

The discretization of the above equation for the retarded time is straightforward. For a given grid, the surface of contact is represented by the corresponding number of cells $N = X_1/\Delta x + 1$, see Fig. 4.11. In this case the cells in the first row (dummy layer) in Fig. 4.5 are used. Let n_{min} denote the leftmost cell and n_{max} the rightmost cell, such that the surface of contact is represented by $n \in \{n_{min}, \dots, n_{max}\}$. Then from (4.27) and assuming a piezoelectric transducer

$$\sigma_{33}^{(n,z)} = -T_0 f^{(z - z_{ret}(n))}, \qquad n \in \{n_{min}, n_{max}\} \tag{4.31}$$

where $z_{ret}(n)$ denotes the time step of the retarded time

$$z_{ret}(n) = \frac{t_{ret}(n\Delta x)}{\Delta t} = \frac{(n - n_{min})\Delta x}{v_{ref}\Delta t} \sin \alpha_{ref} \tag{4.32}$$

The above discussion has focused on modelling an angled (unangled) transducer resulting in a linear retardation along the surface of contact. Another interesting and more general concept is that of a phased array. This may basically be viewed as a transducer consisting of an array of elements which may be controlled individually. As an example of this, the sound field from a focusing transducer will be shown later.

4.10 A model of the transducer as receiver

When the transducer functions as a transmitter, an electric signal is converted to a mechanical traction vector at the surface of contact. In the reverse situation, when the transducer functions as a receiver, the mechanical field at the surface of contact produced by incoming echoes are converted to an electric signal for detection.

When modelling the A-scan of a receiver, we shall as in the previous section, consider only the mechanical information below the transducer. Again, the transducer is positioned at the upper horizontal boundary and due to the fluid coupling between the material and transducer only normal stress components are transferred. As the surface is stress-free, from (4.23) we may consider the normal component v_3 of the velocity field to the surface. This may seem more natural, as the v_3 is defined right on the boundary. The A-scan signal is then modelled as the integral of the v_3-component over the surface of contact

$$A(t) = \int_{x_1^{min}}^{x_1^{max}} W(x_1) v_3(x_1, t - t_{ret}(x_1))\, \mathrm{d}x_1 \tag{4.33}$$

The retarded time is included in the case of an angled transducer and equals the time it takes for the transmitted longitudinal field to propagate from the surface of contact to the piezoelectric element, i. e. through the wedge. This is merely the reverse situation as compared to the angled transmitter in the previous section. In the discrete case, (4.33) is approximated by (setting $W(x_1) = 1$)

$$A(t) = \frac{X_1}{N} \sum_{n=n_{min}}^{n_{max}} v_3^{(n, z - z_{ret}(n))} \tag{4.34}$$

This very simple model of the transducer as a receiver differs from a real receiver in several ways. First, the above assumptions imply that the presence of the receiver at the surface doesn't influence the field, i. e. it is an ideal observer. Another issue, related to the first, is that of a stress free surface beneath the transducer resulting in all the energy being reflected. In a real situation, what is detected is the part of the energy being transmitted across the surface of contact. Thus the v_3-components used in this model are larger in magnitude as they contain both the incident and the reflected field. In fact, from classical textbooks on the subject e.g. [22], in the case of an incoming longitudinal wave, the incoming and reflected fields will give raise to twice the amplitude of the incoming field in the material. This must be taken into account, when interpreting the A-scan. One attempt to overcome this problem would be to consider an absorbing boundary below the transducer. Absorbing boundary conditions in general have been considered in [31–35]. If only relative amplitudes are considered this problem is expected to be negligible. As we shall be concerned with this case in the remaining part of the thesis, the attention will be restricted to the form (4.34) using a stress free boundary. Another important issue relevant when considering angled probes is that of the phase. (4.34) is only valid for waves incident on the transducer with the angle α_{ref}, since the calculation of the retarded time is based on this angle. For incident waves with another angle, the phase (time delay) is not correctly modelled. These problems will be investigated later in chapter 5.